CIRP Journal of Manufacturing Science and Technology 64 (2026) 79–91

Contents lists available at ScienceDirect

CIRP Journal of Manufacturing Science and Technology

journal homepage: www.elsevier.com/locate/cirpj

Melt pool geometry control of Ti-6Al-4V utilizing multi-energy source laser-arc + wire directed energy deposition

James Wainwright [a,*], David Rico Sierra [a], Alec Davis [b], Stewart Williams [a], Jialuo Ding [c]

[a] Welding and Additive Manufacturing Centre, Cranfield University, MK430AL, United Kingdom
[b] Department of Materials, The University of Manchester, M139PL, United Kingdom
[c] WAAM3D Limited, Thornton Chase, Milton Keynes MK14 6FD, United Kingdom

ARTICLE INFO

Keywords:
Wire + arc additive manufacturing
Multi-energy source
Thermal control
Bead geometry control
Process control

ABSTRACT

This study investigates the applicability of a novel laser-arc multi-energy deposition of Ti-6Al-4V with independent control of bead geometry and thermal input. A plasma transferred arc is used to generate an initial melt pool and melt wire feedstock, before controlled lateral elongation of the melt pool via a fiber laser and galvo scanner. The applicability to Ti-6Al-4V was first investigated using deposition parameters previously identified. Once successful bead geometry control was achieved, process parameters more conducive to wire directed energy deposition were investigated. This included investigation of the energy per unit area required to achieve accurate deposition of Ti-6Al-4V with minimal penetration and investigation into scanning strategy. In each case, optical microscopy was conducted and analysis of the bead geometry, penetration and heat-affected zone considered to determine the effect of each parameter change. The results demonstrated that independent control of bead geometry and thermal input could be achieved, allowing deposition of Ti-6Al-4V at a desired scan width and layer height and providing a framework for future multi-energy source directed energy deposition of Ti-6Al-4V.

1. Introduction

Direct energy deposition (DED) additive manufacturing (AM) processes have come under intense academic and commercial scrutiny given their undeniable benefits when compared to traditional manufacturing techniques such as casting, subtractive manufacturing and forgings [1]. These benefits include a reduction in cumulative energy demand, cost reduction and design freedom with respect to complex geometry and microstructural properties [2–4]. During metal additive manufacturing (MAM), metallic components are created through the successive melting or sintering of tracks layer-by-layer using a laser, arc or electron beam energy source and wire or powder feedstock [2]. The deposition of large-scale components such as those associated with aerospace sector, are well suited to the wire + arc additive manufacturing process (WAAM). This process provides substantially high deposition rates, depositing in kilograms per hour and does not typically suffer from process induced porosity [4,5]. A multi-energy source (MES) wire-DED process is one that deposits components with a wire feedstock and multiple thermal energy sources, typically a combination of arc and laser energy sources. The purpose of combining energy sources is to mitigate limitations and combine advantages of the respective energy sources [6].

Conventional arc energy sources used for WAAM include plasma transferred arc (PTA) [7], metal inert gas (MIG) [8] and tungsten inert gas (TIG) [9]. Specific configurations such as cold metal transfer (CMT) [10], pulsed-TIG [11] and pulsed-PTA [12] exist. However, all arc processes face similar limitations with respect to bead geometry control, which is a reliance on changes to heat input. An inversely proportional relationship exists between arc energy and bead geometry, such that neither can be independently manipulated [13]. Additionally, this ensures that the microstructure generated is invariably linked to the bead geometry as a consequence of the heat input [14,15]. It is typical of WAAM processes to generate preforms rather than near net-shape components because of the high deposition rate achieved [16].

Conventional laser additive manufacturing processes incorporate the use of CO_2, neodymium-ytterbium-aluminium-garnet (ND:YAG), fibre and diode lasers. Each type of laser operates at a specific wavelength, dictating the energy absorptivity for different materials [17]. In comparison to arc energy sources, laser energy sources typically generate small melt pools, as a consequence of concentrating their energy in small

* Corresponding author.
E-mail address: j.c.wainwright@cranfield.ac.uk (J. Wainwright).

https://doi.org/10.1016/j.cirpj.2025.11.008
Received 15 April 2025; Received in revised form 2 November 2025; Accepted 22 November 2025
Available online 3 December 2025
1755-5817/© 2025 The Authors. This is an open access article under the CC BY license (http://creativecommons.org/licenses/by/4.0/).

beam diameters to generate high penetration. During laser AM, it is not uncommon for the laser to be defocused to increase melt pool diameter, this transitions the keyhole operation to conduction mode, giving comparatively larger and shallower melt pools conducive to AM [18]. Typically, the melt pool remains smaller than arc processes and laser processes exhibit higher cooling rates than WAAM but benefit from higher shape fidelity [16]. In comparison to arc processes, laser processes have the ability, through beam profiling [13], to alter the distribution of energy across the beam area giving greater control of bead geometry for a fixed energy input. The combination of arc and laser energy sources provides the opportunity for the high deposition rate achievable in WAAM, whilst benefitting from melt pool shape control and improved part fidelity from laser AM [6]. A substantial proportion of MES laser-arc processes use a stationary or oscillating laser leading the arc, operating in a keyhole mode to improve shape fidelity.

Ma et al. [19] investigated the use of an oscillating laser leading a pulsed CMT arc process to deposit Al-6Mg-0.3Sc. The laser was oscillated at 200 Hz across a 2 mm width, in a circular pattern operating in keyhole mode through a 0.4 mm beam diameter. The results demonstrated that the surface roughness decreased by 34 % and effective wall width increased by 20 %. This can be attributed to the increase in melt pool area as a consequence of the increased heat input from the combined energy sources, reducing the overall surface curvature and increased depth of penetration. The oscillation provided a stirring effect within the melt pool interrupting the fluid flow, which provided an environment for epitaxial dendritic growth to be disrupted by dendrite fragmentation. Analysis of the grain boundary misorientations demonstrated that the grain boundaries followed the Mackenzie distribution [20] for polycrystals. Therefore, a fully equiaxed grain structure that removed anisotropic tensile properties was deposited. An additional benefit from the generation of the keyhole combined with stirring, was to allow gases that would be usually trapped to escape the melt pool, reducing porosity by 71 % compared with single energy source CMT deposition of the same alloy.

A similar response was reported by Gong et al. [21] when conducting an equivalent oscillated laser-arc process for the deposition of 316 stainless steel. This study considered the use of a stationary laser leading the arc for comparison to the oscillated laser-arc and WAAM processes. When the trailing laser was stationary, no reduction in porosity was observed. Nor was there a breakdown of the columnar grain structure compared with the oscillated sample confirming the effect of oscillation on the melt pool flow dynamics to transform the morphology of the grain structure and prevent porosity. Tensile anisotropy was eliminated for the oscillated laser-arc process, whilst significant vertical and horizontal differences were recorded for the WAAM and stationary laser process, as a consequence of the columnar grains. However, whilst beneficial to the grain structure and porosity, this method reduces process efficiency, by generating a large area of remelting [6].

Conversely, researchers such as Kapil et al. [22] have found benefits in utilizing a stationary laser-arc MES system, where the laser leads the melt pool. During the deposition of HT780 MAG wire, the addition of the stationary laser increased the size of the melt pool and prevented spatter from being generated during a back-fed CMT process. Their results demonstrated that the bead height was maintained regardless of process parameter variation, recording only a difference in the bead width and penetration depth. However, the results are somewhat misleading. A significant level of undercut can be observed which was taken into account as part of the bead geometry measurements, demonstrating that the process is far from being optimized and that the melt pool flow was insufficient. For a fixed deposition rate, with adequate melt pool flow, the increase in bead width would lead to a reduction in bead height. This has been demonstrated by Wang et al. [23], who investigated the applicability of a plasma arc-laser hybrid for the deposition of Ti-6Al-4V.

Wang et al. [23] studied the effect of various laser and arc process parameters on the bead geometry during a MES laser-arc hybrid process, where the laser was leading the PTA melt pool. In this study when the total heat input, as a result of arc or laser energy increased, the bead height decreased as bead width increased, as expected, unlike the findings of Kapil et.al. [22]. Wang et al. [23] also demonstrated that the beam diameter had little effect on the bead shape despite being increased by a factor of 3, as the total energy input remained constant. [24] noted a similar effect when studying the laser stabilization of a CMT arc process utilizing a laser concentric with the arc center. They determined that the surface roughness was stabilized, and that total energy input of the laser was responsible for the bead width and not beam diameter. However, neither considered that as the beam diameter increased, with a constant laser power, there would be a corresponding reduction in power density, which would likely result in different localized cooling rates and microstructures despite having the same total heat input. Ultimately, the results of the study by Wang et al. [23] identified that the optimum configuration for the laser-arc MES process is when the PTA is used to melt the wire feedstock, and the melt pool size is controlled via the laser. This is a consequence of the higher melting efficiency during WAAM compared to laser AM [6].

Wang et al. [25] further investigated the deposition of Ti-6Al-4V with a dual laser-arc MES process having identified an optimal configuration, with the PTA used to melt the wire feedstock and laser to control melt pool shape. Dual stationary lasers positioned to the side and rear of the melt pool were used to elongate the total melt pool area. In comparison to the previous MES processes mentioned, Wang et al. [25] operated in conduction mode. This is more conducive to additive manufacturing by improving process efficiency through reducing remelting [6]. Their results demonstrated that independent control of the bead geometry and deposition rate could be achieved in the deposition of Ti-6Al-4V. However, it was imperative that a quasi-steady state melt pool was generated. When independent melt pools from the multiple energy sources were formed, the feedstock material from the PTA melt pool was unable to successfully flow, generating poor surface quality and lack of fusion defects. Wang et al. [25] successfully deposited several walls up to 18.6 mm wide, whilst maintaining negligible surface roughness. Whilst this work did not explicitly consider the microstructure generated, it was evident in the optical macrographs that a columnar prior-β grain structure existed.

Hao et al. [26] also demonstrated the importance of maintaining a quasi-state melt pool to form large melt pool widths. They investigated the use of an oscillating laser on weld bead shape. Their results demonstrated that deposition of a sawtooth pattern is generated if the oscillating frequency is not large enough to incur sufficient overlapping. Whilst not discussed, it can be deduced that the increase in oscillating frequency would ensure that the melt pool had not solidified before the return path of the laser ensuring a continuously wide quasi-steady state melt pool as highlighted by Chen et al. [13].

Previous literature has largely focused on the improvement of process stability and bead surface quality rather than the ability to independently control the melt pool shape and thermal input, thus mostly considering static additional heat sources. Chen et al. [13] presented a novel MES process to enable independent control of bead width and bead height for steel that may be applicable to controlling melt pool shape of titanium alloys during AM. Through the application of a scanning laser and arc MES process, the PTA energy source was used to form an initial melt pool and melt the wire feedstock. A fiber laser and galvo-scanner were used to extend the melt pool behind the arc to a specified width, ensuring a quasi-steady state melt pool was generated. With this arrangement they were able to demonstrate that independent control of bead width and bead height could be obtained for mild steel, with dynamic width control during deposition. It was demonstrated that the bead width and travel speed were dependent on the scanning width selected, whilst the bead height was controlled by the wire feed speed (WFS). This demonstrated that melt pool geometry could be manipulated independently of thermal input, something that cannot be done in single energy source deposition. This is highly useful during the deposition of AM components where complex tool path strategies are

considered for various features and thicknesses.

The purpose of this paper was therefore to determine the applicability and relevant parameters of the novel scanning laser and arc MES process proposed by Chen et al. [13] to the deposition of Ti-6Al-4V, noting the differences in the thermal properties such as viscosity, thermal conductivity and surface tension between steel and titanium [27] and their respective microstructural characteristics. The thermal conductivity of Ti-6Al-4V is reported to be~ 7 W/mK as compared to mild steel at ~50 W/mK and their viscosity at melting temperature has been reported as ~4.7 mPa.s for titanium compared to ~6 mPa.s for mild steel [28–31], causing variation in their weldability. If successful, this would enable independent control of the melt pool shape and thermal input, providing a useful process and framework for the deposition of complex Ti-6Al-4V components and features with various geometries, with the potential to negate complex toolpath planning and provide a mechanism to investigate the metallurgical relationship between melt pool shape and microstructure as posited by Davis et al.[32].

1.1. Theory

To understand the influence of the processing parameters on the deposition, several fundamental parameters first require definition, as discussed in the following sections.

1.1.1. Energy per unit area

The MES process allows the configuration of the laser energy source scan path, ultimately this can be used to control the melt pool geometry [13,23,24] in terms of melt pool width and depth. During the scanning laser process, a sawtooth pattern is formed as the melt pool advances as demonstrated in Fig. 1. This means that a specific point is irradiated numerous times by the laser during deposition and is determined by the beam diameter and scan frequency, this is defined by Eqs. 1–3.

To calculate the number of interactions over a specific point, two calculations initially need to be made, the scanning frequency (Eq. 1) and the amplitude of the sawtooth pattern (Eq. 2). Subsequently, the number of interactions can be calculated by Eq. 3 [13].

$$F_s = \frac{v_s}{2w_s} \ldots\ldots \quad (1)$$

Where $\boldsymbol{F_s}$ represents scanning frequency, $\boldsymbol{v_s}$ represents the scanning velocity and $\boldsymbol{w_s}$ represents the scanning width.

$$A_O = \frac{v_a}{F_s} \ldots\ldots \quad (2)$$

Where $\boldsymbol{A_O}$ represents the amplitude of the oscillation pattern and $\boldsymbol{v_a}$ represents the travel speed during deposition.

$$n_i = \frac{B_d}{A_O} \ldots\ldots \quad (3)$$

Where $\boldsymbol{B_d}$ represents the beam diameter.

However, the process requires the generation of a quasi-steady state melt pool to be maintained. It is possible to simplify this scanning laser interaction with the substrate as an equivalent bar heat source also proposed by Chen et al. [33]. This is illustrated in Fig. 2, where $\boldsymbol{A_O}$ represents the amplitude of oscillation (this is equivalent to the laser beam diameter) and the desired scan width $\boldsymbol{w_s}$ as previous.

In the case of a fixed travel speed, the interaction time of the heat source with the substrate can be defined by Eq. 4, assuming that the galvo-scanner moves at a constant velocity.

$$t = \frac{A_0}{v_a} \ldots\ldots \quad (4)$$

Where $\boldsymbol{v_a}$ represents the linear travel speed.

This provides an interaction time dependent on the scanning amplitude allowing proper comparison of the energy deposited with various travel speeds and scanning amplitudes. As may be observed, the linear travel speed is a key factor in determining the energy being deposited to the substrate. The scanning area and interaction time determines the energy deposited by the equivalent heat source and can be calculated by Eq. 5.

$$E = \eta_L P \quad \times t \ldots\ldots \quad (5)$$

Where ($\boldsymbol{E}$) represents the total energy deposited, ($\boldsymbol{P}$) the laser power, $\boldsymbol{\eta_L}$ represents laser absorptivity coefficient and ($\boldsymbol{t}$) and interaction time calculated in Eq. 4, an absorptivity coefficient of 0.45 used for Ti-6Al-4V based upon existing literature [34,35].

This provides the total energy deposited by the equivalent heat source in the time it takes to transverse the full length of the scanning amplitude. As varying scanning widths were explored in this research, a genuine comparison between the energy deposited by the scanning laser can be accounted for using Eq. (6) to calculate the energy deposited per unit area.

$$E_A = \frac{E}{Aw_s} \ldots\ldots \quad (6)$$

Where $\boldsymbol{E_A}$ represents the energy per unit area.

1.1.2. Bead geometry prediction

With independent control of the bead geometry from the energy input, the relationship can be explained geometrically, based upon the rate of deposition to provide a bead geometry prediction. Consider Eq. 7, which is a standard expression of the deposition rate [36], i.e. the volume of wire fed per second.

$$R = \frac{\pi d^2}{4}.WFS.\rho \ldots\ldots \quad (7)$$

Where $\boldsymbol{WFS}$ represents wire feed speed, $\boldsymbol{d}$ the feedstock diameter, $\boldsymbol{\rho}$ represents the wire density and $\boldsymbol{R}$ the deposition rate. Correspondingly, the deposition rate may also be considered as an expression of the cross-sectional area of the deposit as seen in Eq. 8. Chen et al. [13] considered this as a rectangle, however, the Ti-6Al-4V MES deposited beads observed were more ovular in nature and so an ovular relationship was considered.

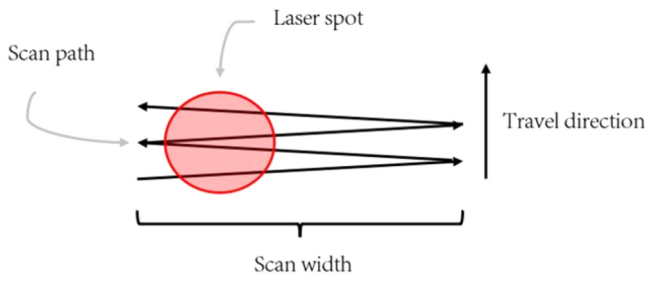


Fig. 1. Sawtooth pattern generated by scanning laser during deposition. Adapted from [13].

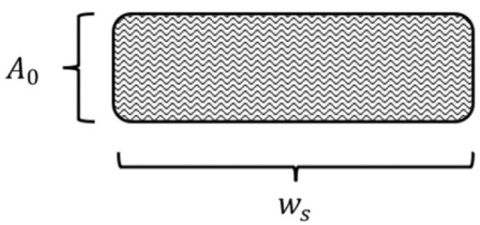


Fig. 2. Illustration of equivalent heat source area generated by scanning laser.

$$R = \pi.\frac{W}{2}.H.v_a.\rho\ldots\ldots \quad (8)$$

Where $\boldsymbol{W}$ represents bead width, $\boldsymbol{H}$ represents bead height and $\boldsymbol{v_a}$ continues to represent travel speed. Deposition rate can now be expressed in terms of the volume of wire fed per second and the deposited geometry as expressed in Eq. 9.

$$\frac{\pi d^2}{4}.WFS.\rho = \pi.\frac{W}{2}.H.v_a.\rho\ldots\ldots \quad (9)$$

Eq. 9 can be used to determine the processing parameters required to deposit a specific bead geometry. For example, by rearrangement in Eq. 10, it can be determined that the scanning width is predominantly controlled by the scanning laser and if the energy per unit area is maintained through for an equivalent $\boldsymbol{wv_a}$, the bead height ($\boldsymbol{H}$) is determined by the $\boldsymbol{WFS}$.

$$H = \frac{d^2}{2}.\frac{WFS}{Wv_a}\ldots\ldots \quad (10)$$

2. Methodology

Several processing parameter conditions were considered during this investigation and will be discussed in detail in their respective sections. In summary, a preliminary investigation with equivalent processing parameters to Chen et al. [13] was conducted to test the applicability of the novel MES system to the deposition of Ti-6Al-4V with no previously identified parameters for Ti-6Al-4V in this manner. Noting the low travel speed of deposition used, subsequent investigation into increasing the travel speed and wire feed speed of deposition to a regime more conducive to additive manufacturing was conducted, consideration into the energy distribution of the scanning laser was also considered and energy per unit area required to achieve suitable depositions characteristics in line with the desired bead geometries and lack of defects such as undercut or ablation.

The experimental setup schematic may be observed in Fig. 3, samples were deposited on to Ti-6Al-4V substrate clamped to an aluminium backing plate. Various substrate sizes were utilized dependent on the scan width and will be detailed in their relevant sections, however given the relatively small size of the welds to the substrate and consistent deposition parameters this is not expected to interfere with the results observed. 3.1 discusses the applicability of the MES method to titanium, 3.2 discusses an increase in travel speed and WFS, 3.3 discusses identification of the energy per unit area and 3.4 discusses the reduction of laser energy at the width center due to the influence of the arc. Deposits were conducted with a single pass, single direction strategy using an Aerotech A3200 controller and 3-axis CNC Aerotech stage gantry system. A PWP Viper MC plasma torch at 15° offset and EWM 352 DC power source were used to create the initial melt pool, trailed by an unpolarized SPI 6 kW continuous wave fiber laser (1.08 μm wavelength) with a gaussian beam profile. Various scan widths were considered and manipulated via an IPG highspeed galvo-scanner controlled by IPGWeld software. A laser-arc offset of 10 mm was used, having been identified as the optimal configuration from Chen et al. [13] where the laser scan width clips the PTA melt pool. A defocused 4 mm beam diameter was used to ensure that the melt pool operation mode was by conduction. Dual Migatronic KT4 wire feeders were used to front feed wire to the center of the arc at an inclination angle of 5° and offset of 10°. All samples were deposited inside a globally shielded environment purged with UN1006 Pureshield Argon and maintained at an oxygen level of $<$ 500 PPM, continuously monitored with a Argweld PurgEye 600. The composition of the wire feedstock used in this study is detailed from the manufacturer and available in Table 1.

During deposition, all samples were monitored via a Xiris XVC-1100 processing camera mounted perpendicular to the melt pool and continuously monitored to ensure process stability, i.e. no erroneous melt pool fluctuations, and a consistent 'droplet' feedstock transfer mode [37]. To ensure high image quality capture, the camera aperture was set to the manufacturer's minimum and a rolling shutter mode with a 10 μs exposure time. A Xiris 50 mm lens with UV filter and spatter protection was used.

Post deposition, cross-sectional samples were extracted for geometrical and microstructural analysis from the central section of each specimen. Samples were mounted in conductive phenolic resin via a hot

Table 1
Wire feedstock composition Ti-6Al-4V (wt%).

O	N	C	Fe	Al	V	Si	H	Ti
0.15	0.008	0.021	0.18	6.14	3.94	0.012	0.0004	BAL

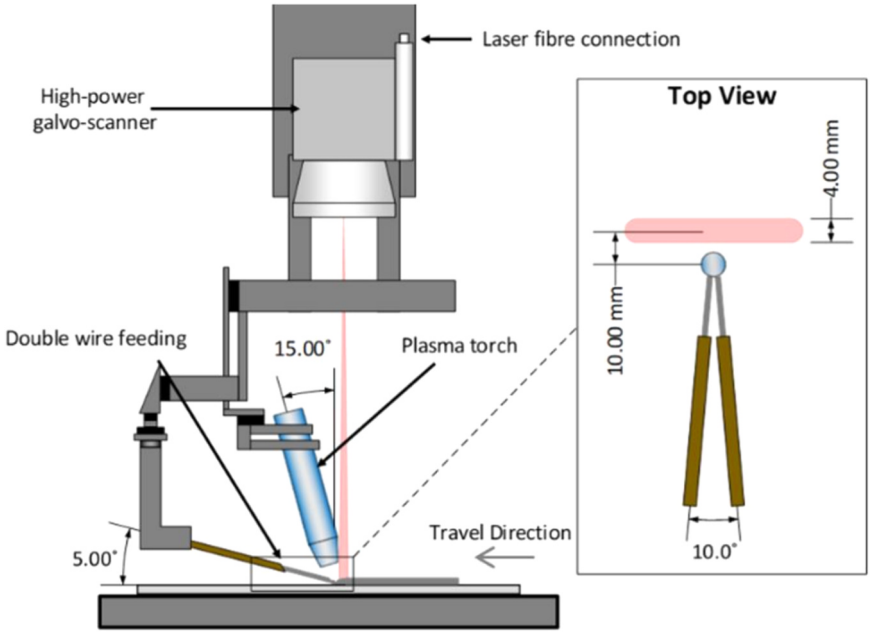


Fig. 3. Experimental setup schematic for MES source system combining PTA and fibre laser with galvo-scanner.

mounting press. All samples were mechanically polished using consecutively higher grades of silicon carbide paper from 240 to 2000 grit, before a final polish using colloidal silica and oxalic acid and etching with Kroll's reagent for ~ 10 s to reveal the α + β microstructure. Optical microscopy was conducted using a Hirox RH-2000 for large area mapping at a magnification of 50x. Geometrical measurements of the melt pool were conducted using AxioVision 4.8. In all cases, bead geometry and microstructure was measured using the definitions described by Brandl et al. [38] as detailed in Fig. 4. Given the propensity for epitaxial columnar growth in Ti-6Al-4V during WAAM [2,39,40], the melt pool penetration depth was taken from the beginning of columnar prior-β grain growth. Whilst this technique is useful, it is somewhat limited as it is dependent on the discretion of the user and quality of macrographs observed. Therefore, there is interpretation within the quantitative results reported, however, this does not detract from the clearly observed trends that are clear. For each geometry measurement, 3 points were taken, and the average is reported. The bead width is taken between the points at which the deposited material becomes higher than the substrate and bead height is taken at the central point of these two points vertically.

3. Results and discussion

3.1. Applicability of scanning laser-arc MES deposition of Ti-6Al-4V

A preliminary investigation of the applicability of the MES system was conducted with Ti-6Al-4V wire feedstock and substrate (100 mm×175 mm x 10 mm) to deposit 80 mm long single bead on plate tracks. Chen et al. [13] successfully demonstrated the independent control of the bead width and bead height with mild steel deposition and as such two parameter sets were selected for replication in Ti-6Al-4V. The purpose of this preliminary investigation (PI) was to identify any processing nuances that may occur when utilizing a different equipment setup and alloy with differing thermal-fluid characteristics [27].

Four samples were deposited per study with a WFS of 5.0, 13.1,18.5 and 23.8 mm/s therefore, 8 samples in total. The process parameters used during this preliminary investigation are detailed in Table 2.

Considering Eqs. 4–6, as the scanning width was increased from 16.5 mm to 20 mm, in order to maintain an equivalent energy per unit area requires the reduction of the travel speed. If the same travel speed were maintained for the 20 mm scan width as the 16.5 mm, the same energy would be shared over a larger area. Therefore, to ensure an equivalent energy per unit area, and thus thermal input, a reduction in the linear travel speed is required as the scanning width is increased. This increases the laser interaction time and thus total energy. This larger total energy is now shared over the greater area to maintain equivalency. The energy per unit area of the samples in PI 1 was calculated as 20.4 kJ/cm^2 and PI 2 as 20.1 kJ/cm^2 using scanning widths of 16.5 mm and 20 mm respectively.

As discussed by Chen et al. [13], to prevent excessive energy in the center of the scan width from the laser where the energy from the arc is also delivered, the scan path was divided into 3 lines. In the central region, where the arc energy was delivered, the scanning speed was increased to the maximum of 16,500 mm/s, minimizing the local interaction time for a fixed distance of 3.5 mm. The scan speed on either side of the central distance remained constant at 500 mm/s. The scan path alternated direction, i.e. left to right and right to left, generating a sawtooth pattern as the melt pool advanced. A schematic is provided in Fig. 5.

For the PI 1 specimens with a 16.5 mm combined scan width, the as-deposited samples and central cross-sectional optical macrographs may be observed in Fig. 6. Inspection of the deposited samples demonstrated a large ovular melt pool shape, as opposed to the rectangular melt pool seen by Chen et al. [13] this infers that the center of melt pool remains hotter than the outer edge with surface tension pulling the material to the center of the melt pool, limiting its spread. However, in respect to applicability it was clear that the melt pool had elongated along the width due to the scanning process as intended. Investigation of the macrographs confirmed the presence of a large heat input from the microstructure. There is a clear large heat affected zone (HAZ) present across the entire substrate thickness, which led to significant prior-β coarsening and a columnar grain structure within the fusion zone. This may be explained by the significantly large heat input that is obtained from a travel speed of 0.8 mm/s [15]. The effect of the large heat input may also be observed by the introduction of porosity in the sample at the deposition surface. This demonstrates that during the course of deposition excessive energy led to ablation of the bead surface and vaporization of the deposited material, which was observed as vapor plumes leaving the surface during deposition [41].

The bead geometry was measured using the definitions outlined by Brandl et al. [38]. As may be observed in Fig. 7, the increase in WFS led to an increase in the bead height from ~ 0.5 mm to ~ 2.0 mm, whilst the bead width remained similar at ~ 27.5 mm. In all cases the measured penetration depth was significantly large at ~ 5.5 mm and as expected the contact angle increased as WFS and thus bead height increased. As to be expected, given that a scan width larger than the arc melt pool width was specified and that the heat input and energy per unit area remained equivalent across all specimens, the same bead width was measured in all cases. The increase in bead width over the specified scan width was not surprising, given the excessive heat input at low travel speeds. The high heat input was also responsible for low process efficiency clearly expressed by the large penetration depth [6].

Both the as-deposited sample and cross-sectional macrographs taken at the center of the deposited sections for the PI 2 specimens may be observed in Fig. 8. A 20 mm combined scan width was used, increasing the scanning distance on the outer edges as compared to PI 1 and travel speed reduced to maintain energy per unit area.

The PI 2 specimens, similar to PI 1, demonstrated a large ovular melt pool shape that was also dominated by surface tension pulling the molten titanium to the center, rather than giving a rectangular melt pool

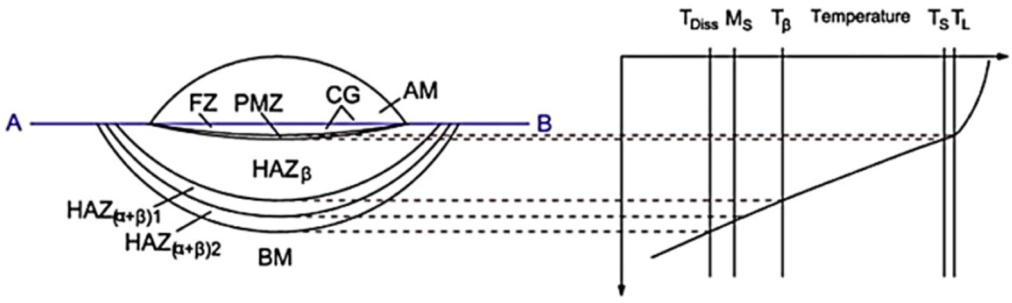


Fig. 4. Correlation of temperature and resulting microstructural zone, used for geometrical measurements of the bead geometry (FZ – Fusion zone, PMZ (Partially melted zone, CG -Columnar growth, AM – Added material, HAZ – heat affected zone, BM – Base metal, T_{Diss} – α dissolution temperature, M_S – Martensite starting temperature, T_S – Solidus temperature, T_L – Liquidus temperature). Adapted from [38].

Table 2
Process parameters utilised during preliminary investigation of MES applicability to Ti-6Al-4V.

ID	Laser power (W)	Arc current (A)	Scan speed (mm/s)	Scan width (mm)	Travel speed (mm/s)
PI 1	3000	140	500_16500_500	6.5_3.5_6.5 (16.5)*	0.8
PI 2	3000	140	500_16500_500	8.25_3.5_8.25 (20.0)*	0.67

* Note the combined scan width in PI 1 = 16.5 mm and PI 2 = 20 mm

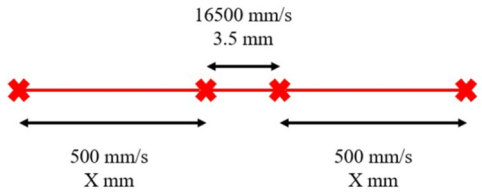


Fig. 5. Schematic of three-line scan strategy to avoid unnecessary energy delivery to scan width centre.

shape. The PI 2 specimens showed an identical geometry and microstructural evolution as PI 1, with an elongated melt pool width and severe prior-β grain coarsening demonstrated by the large primary HAZ across the thickness of the substrate for each specimen. The PI 2 specimens also demonstrated evidence of vaporization [41] by the formation of tiny pores at the surface of the deposited beads. In the case of PI 1 and PI 2 specimens, final bead geometry appeared ovular in nature when considering the bead cross-section. The bead geometry of the PI 2 specimens may be observed in Fig. 9.

The bead geometry results from the PI 2 specimens show the same trend as the results from the PI 1 specimens. As WFS increased, an increase in the bead height from ~ 0.5 mm to 2.0 mm was recorded, whilst the bead width remained similar at ~ 29.0 mm. The penetration depth was similar at ~ 5.5 mm and the contact angle increased with WFS and thus bead height increased. Given an equivalent energy per unit area across both the PI 1 and PI 2 specimens, the same penetration depth was expected, however, the heat input from the arc would be larger in PI 2 as a consequence of the reduced travel speed [42]. No observable change in penetration depth was observed from this, however, the reduction in travel speed from 0.8 mm/s to 0.67 mm/s was negligible and thus no obvious measurable variation in the penetration depth was expected.

In both the PI 1 and PI 2 specimens, the total measured melt pool width was greater than the desired scan width indicating an excessive heat input. A similar effect was observed by Chen et al. [13], however the effect was not as severe. This highlights the difference in the thermal properties of the steel and titanium during MES laser-arc welding for the same deposition conditions, specifically the difference in thermal conductivity, which is much lower in titanium, causing heat accumulation and excessive 'over-melting'. Regardless, this effect corroborated with previous research conducted by Pardal et al. [24], that demonstrated that the heat input from the laser energy source during a MES system can increase the melt pool geometry. Nevertheless, it can be observed from Fig. 10 that despite an excessive heat input, independent control of bead geometry had been achieved, with bead height being maintained for differing bead widths. Overall results from the PI 1 and PI 2 specimens confirm the applicability of the novel MES process proposed by Chen et al. [13], warranting further investigation.

3.2. Increased travel speed and wire feed speed during deposition

During the preliminary investigation (PI) study, as a consequence of the slow linear travel speed, an excessive heat input led to excessive melting causing the bead width to be greater than the desired scan width. The purpose of this subsequent study was to increase the travel speed and WFS to a workable regime with respect to WAAM, that typically deposits at speeds upwards of 2 mm/s and where bead height is

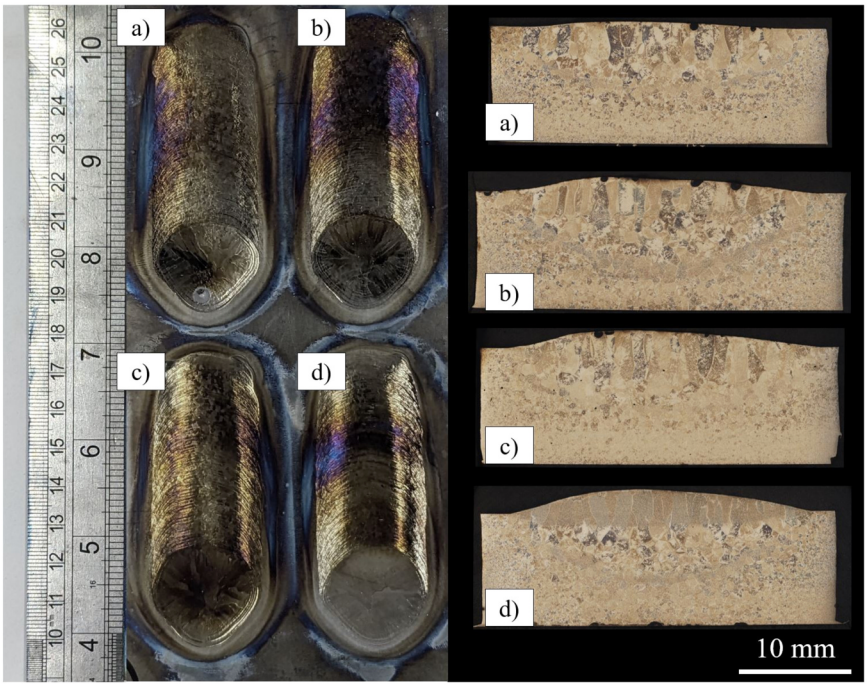


Fig. 6. (L)As-deposited Ti-6Al-4V specimens of PI 1 using MES system with scan width of 16.5 mm with multiple wire feed speeds of a) 5.0 mm/s, b) 13.1 mm/s, c) 18.5 mm/s, d) 23.8 mm/s. (R) Etched cross-sections from deposition centre.

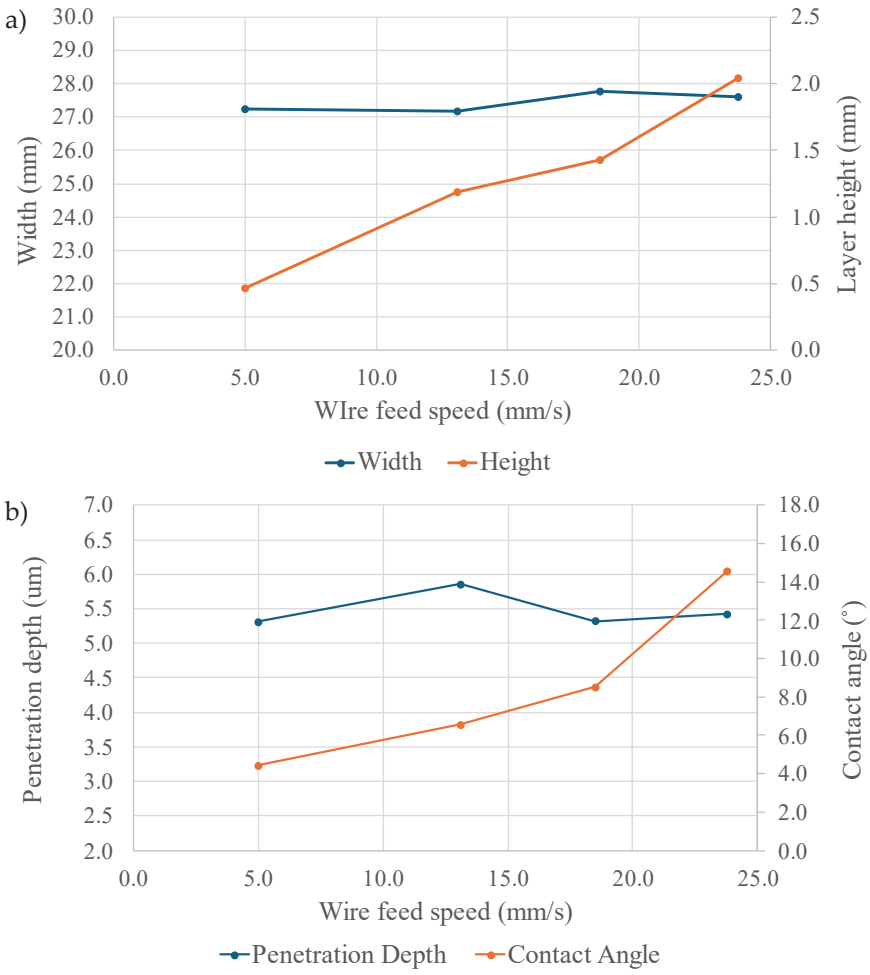


Fig. 7. Bead geometry measurements from cross-sections of PI 1 specimens a) Bead width and height, b) Penetration depth and bead contact angle with substrate.

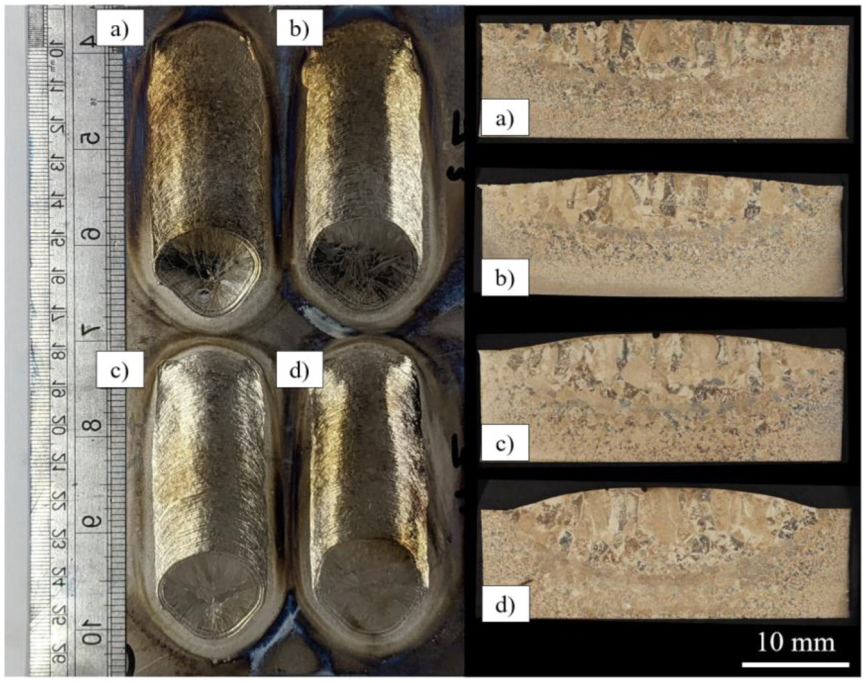


Fig. 8. (L) As-deposited Ti-6Al-4V specimens of PI 2 using MES system with scan width of 20 mm with multiple wire feed speeds of a) 5.0 mm/s, b) 13.1 mm/s, c) 18.5 mm/s, d) 23.8 mm/s. (R) Etched cross-sections from deposition centre.

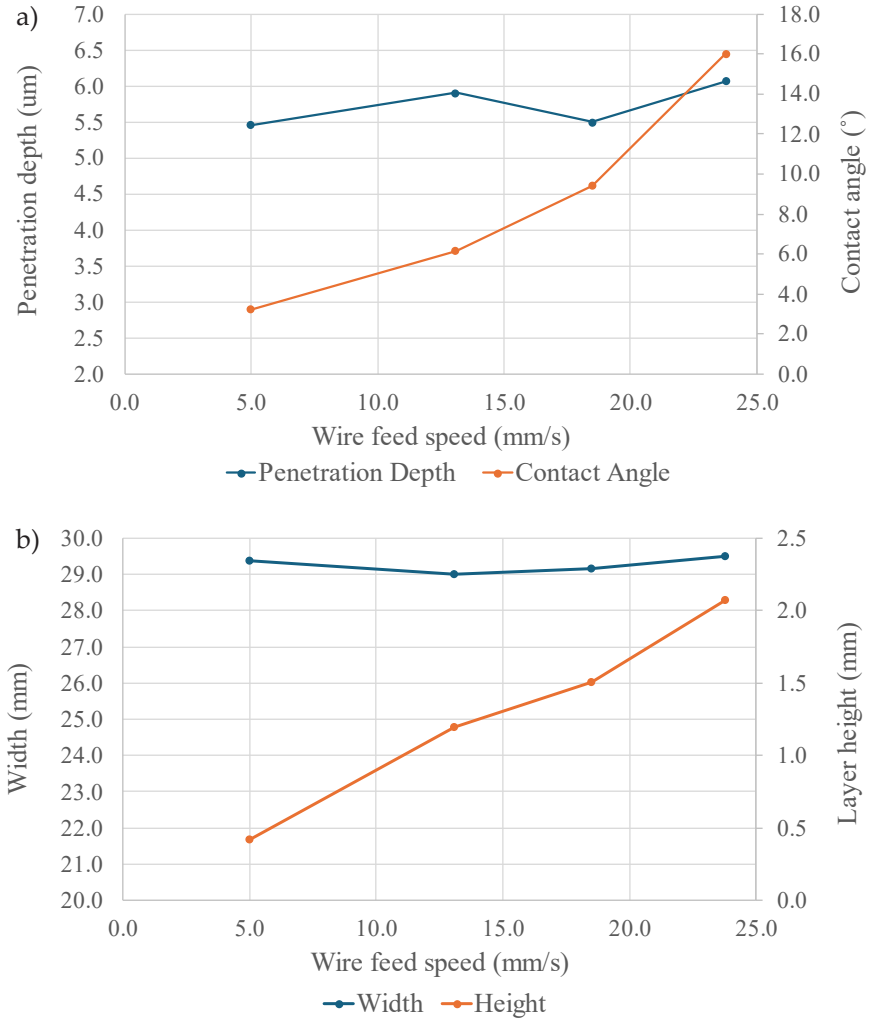


Fig. 9. Bead geometry measurements from cross-sections of P1 2 specimens a) Bead width and height, b) Penetration depth and bead contact angle with substrate.

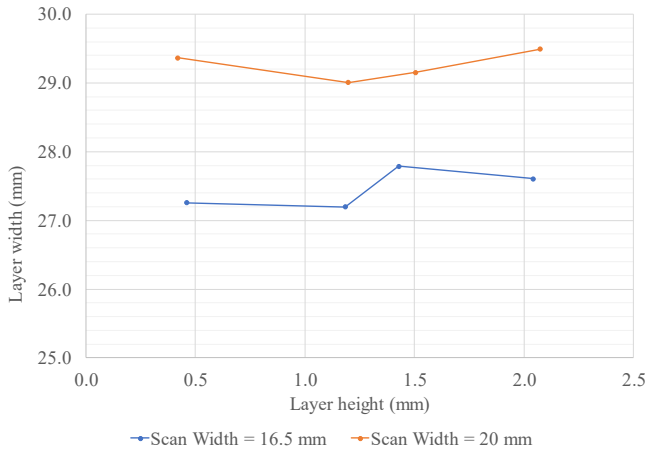


Fig. 10. Comparison of bead geometry for PI 1 and PI 2. Note that bead width and height can be controlled independently.

greater than penetration depth [2] and no over melting occurred. As denoted in Eqs. 3–6, to maintain an equivalent energy per unit area to the preliminary investigation, with travel speed increased and all other parameters remaining constant, a decrease in scan width to 6.75 mm was required, resulting in an energy per unit area of 20.0 kJ/cm^2. Given the shorter scan width, a single path scan strategy was used at 500 mm/s due to limitations of the galvo-scanner. Four specimens were deposited with a WFS also more representative of WAAM at 24.40 mm/s; 37.97 mms/s; 45.03 mm/s and 51.87 mm/s. This range was chosen to ensure that independent bead geometry was maintained across varying WFS. The substrate used in this study was Ti-6Al-4V (25 mm×100 mm x 10 mm). Single track 80 mm long beads were deposited. The process parameters used may be observed in Table 3.

From the etched light optical macrographs of the central cross-sections in Fig. 11, it may be observed that the height of the bead increased with WFS as expected, however the bead width remained larger than the scan width. In comparison to PI 1 and PI 2 samples, the depth of penetration appears to have decreased, alongside the size of the primary and secondary HAZ [38], which is a result of the decreased heat input as travel speed increased. It may be qualitatively observed that the size of penetration and HAZ was of similar sizes across all specimens, regardless of WFS, and was to be expected given an equivalent heat

Table 3
Process parameters utilised for increased wire feed speed and travel speed of MES deposition of Ti-6Al-4V.

ID	Laser power (W)	Arc current (A)	Scan speed (mm/s)	Scan width (mm)	Travel speed (mm/s)
TS 1	3000	140	500	6.75	2.0

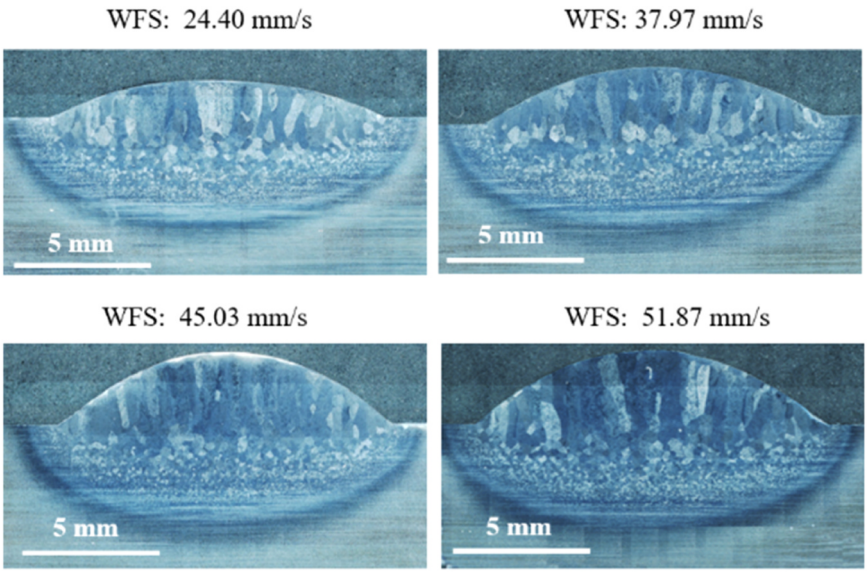


Fig. 11. Etched cross sections of Ti-6Al-4V MES deposited specimens at varying WFS and increased travel speed.

input. As expected during the deposition of Ti-6Al-4V [1,43–45] the grain structure demonstrated a columnar prior-β grain morphology. The geometry of the deposited bead may be observed in Fig. 12.

Despite the increase in travel speed to 2 mm/s, the independent control of the bead width and bead height was maintained. The contact angle and build height were larger than the preliminary investigation specimens due to an increase in WFS and deposition rate. The depth of penetration was significantly improved in relation to the preliminary investigation, reducing to ~ 2.25 mm from ~ 5.5 mm. This occurred through the increased travel speed and consequent reduction in heat input. The bead geometry measurements for the bead width and bead height of the TS 1 specimens also demonstrated alignment with the intended geometric bead shape. The bead shape control prediction (Eq. 9) is therefore a useful tool to identify processing parameters and identify melt pool shape and bead geometry using the MES system. For example, when considering the actual bead width in place of the scanning width (until such a point where desired scan width is achieved) to predict the bead height there is strong correlation with the actual deposited height. Alternatively, when using the actual bead height to predict the bead width, the prediction is also accurate, as may be observed in Fig. 13.

However, as reported the bead width remained significantly greater than the desired scan width. As discussed by previous studies [22–24], the addition of the laser energy is used to increase the size of the melt pool and in this study was responsible for generating the elongation of the melt pool. However, the energy per unit area being delivered was too large and was generating a melt pool significantly larger than the desired width. Therefore, an investigation into the required energy per unit area to achieve the desired scan width was required for the deposition of Ti-6Al-4V, to ensure that the melt pool shape can be controlled accurately.

3.3. Identification of required energy per unit area

Clearly demonstrated, to achieve the desired scan width, the correct energy per unit area required must be identified to prevent over-melting. During this investigation two scan widths (13.5 mm and 16.5 mm) were investigated, through the deposition of Ti-6Al-4V with fixed process parameters excluding travel speed. The travel speed was systematically increased from 3 mm/s to 9 mm/s in 1 mm/s increments with a WFS of 58.2 mm/s maintained throughout. A single line scan strategy was used at 500 mm/s. In relation to Eq. 6, this lowered the energy per unit area delivered by the laser through a reduction in the interaction time as linear velocity increased. Additionally, the arc current was lowered compared to the previous studies to reduce the maximum penetration depth. This allowed identification of the energy per unit area required to achieve the desired bead width, without excessively overheating the substrate and erasing the differing microstructural areas. The process

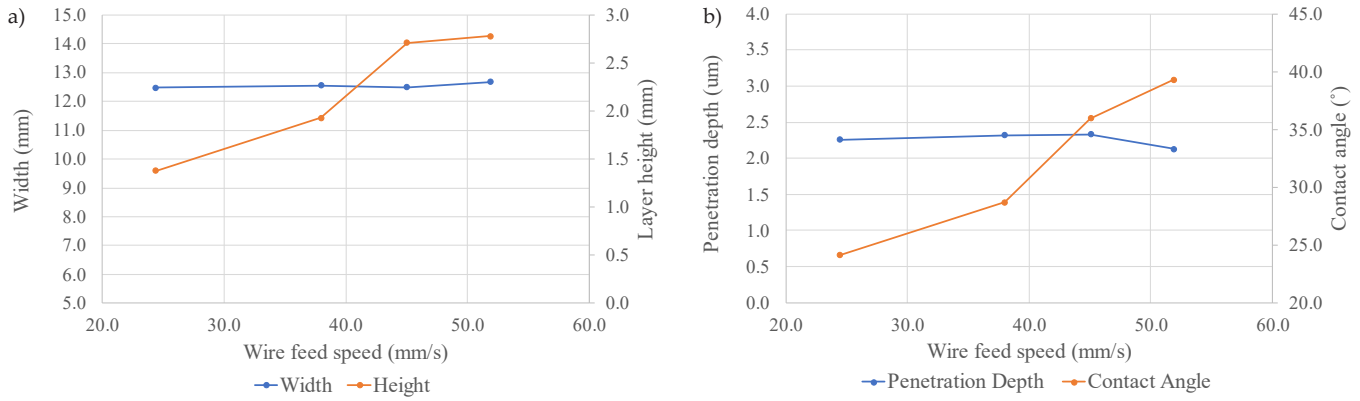


Fig. 12. Bead geometry measurements from cross-sections with increased travel speed specimens (a) Bead width and height, (b) Penetration depth and bead contact angle with substrate.

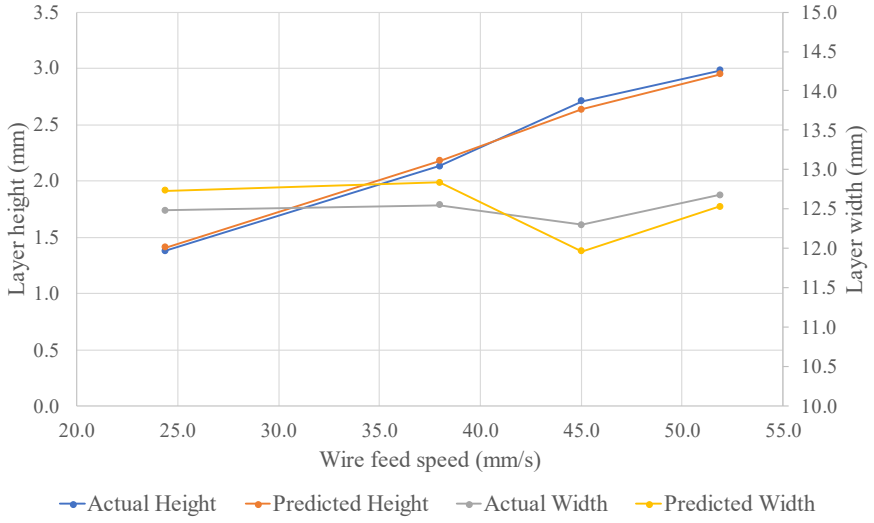


Fig. 13. Bead geometry prediction vs actual bead deposited geometry using bead shape prediction from Eq. 9. Note that the relationship between predicted geometry and actual geometry is closely related meaning the prediction can be used to set process parameters. In this case the scanning width has been replaced by the actual bead width.

parameters used in this study are detailed in Table 4 and the etched optical light macrographs may be observed in Fig. 14.

It may be observed from Fig. 14 that, for both scanning widths, as the travel speed of deposition was increased there was a distinct change in bead geometry. Most notably in the bead height, penetration depth and primary HAZ. As the WFS was fixed, the decrease in bead height was attributed to the reduction in deposition rate as the travel speed increased. The reduction in penetration depth and primary HAZ can be attributed to the reduction in heat input from the arc and lower energy per unit area of the laser [23]. When the travel speed reached 8 mm/s for the 13.5 mm scan width in the EPU 1 study at 13.5 mm scan width, the deposited material did not appear to have fully spread and the bead shape was triangular. A comparable observation is made in the 16.5 mm scan width in EPU 2 from 7 mm/s upwards. A similar response is noted in Kapil et al. [22] where the molten material would not sufficiently spread and can be attributed to the energy per unit area being too low. The bead geometry for both the EPU 1 and EPU 2 specimens may be observed in Table 5 and Table 6 respectively.

It may be observed that as the travel speed increased, the energy per unit area decreased. This was a consequence of a shorter interaction time as linear velocity increased and the scanning speed and width remained constant reducing the amount of energy delivered. During the deposition of the EPU 1 13.5 mm scan width specimens, the scan width and measured width almost converged (highlighted in red) at 2857 J/cm^2. The same observation can be made for the EPU 2 16.5 mm specimens, where the scan width and bead width converged (highlighted in red) at 2727 J/cm^2. Therefore, it may be deduced that when considering a coupling efficiency of 0.45, to ensure that the control of the bead width can be achieved for a desired scan width, an energy per unit area of ~ 2.7 – 2.8 kJ/cm^2 must be maintained. Consequently, in relation to the bead shape prediction (Eq. 9), the measured bead heights for the respective energy per unit area's identified, corresponded to a predicted 13.16 mm bead width for EPU 1 and 16.43 mm bead width for EPU 2 prediction, demonstrating a strong correlation with the measured bead widths of 13.66 mm and 16.78 mm, and usefulness of the bead prediction equation once bead shape control is achieved.

Table 4
Process parameters of samples deposited for identification of the required energy per unit area to achieve desired bead width.

ID	Laser power (W)	Arc current (A)	Scan speed (mm/s)	Scan width (mm)	Wire feed speed (mm/s)
EPU 1	3000	105	500	13.5	58.2
EPU 2	3000	105	500	16.5	58.2

3.4. Reduction of laser energy at scan width centre

As previously discussed, a significant amount of energy is delivered to the center of the scan path when a single line strategy is employed due to the overlapping of the arc and laser heat sources. However, during the formation of the quasi-steady state melt pool between the arc and laser, there is no requirement for additional laser energy in the melt pool center as this is provided by the arc [13]. Therefore, the removal of laser energy over the arc melt pool area was investigated with equivalent process parameters to EPU 1 and EPU 2 listed in Table 4 for direct comparison to the single line strategy. Three travel speeds were considered, 4 mm/s, 5 mm/s and 6 mm/s for each scan width (13.5 mm and 16.5 mm). The scan strategy used, was equivalent to the preliminary investigation as illustrated in Fig. 3. A 3.5 mm gap was maintained at the center of the scan width and each side of this a 5 mm and 6.5 mm length used for the combined 13.5 mm and 16.5 mm scan width respectively. The etched light optical macrographs may be observed in Fig. 15.

No discernible qualitative difference between the specimens deposited with the 3-line scan strategy to their equivalent single line strategy from the EPU 1 and EPU 2 study could be seen. Quantitative analysis of the bead geometry is reported in Table 7 and Table 8, comparing the geometries of the single line strategy from EPU 1 and EPU 2 to the 3-line strategies in this study.

As may be observed, with respect to the 13.5 mm scan width, regardless of whether a single line or multi 3-line scan strategy was used, the bead geometry remained relatively consistent across the bead width, height, penetration depth and primary HAZ. Suggesting that the 3-line scan strategy had little effect on reducing heat input and did not alter the deposition characteristics significantly. In the case of the 16.5 mm scan width, a minor impact of the 3-line strategy could be noticed. In the case of bead width and bead height the geometry remained consistent. In the case of the primary HAZ, the size remained consistent until the 6 mm/s case where a 0.3 mm difference (16 % decrease) in HAZ could be determined in the 3-line scan strategy. In the case of the penetration depth, a consistent ~ 0.2 mm lower penetration depth was achieved in all cases for the 3-line scan strategy, inferring that the removal of the laser energy at this point prevented a small quantity of remelting and

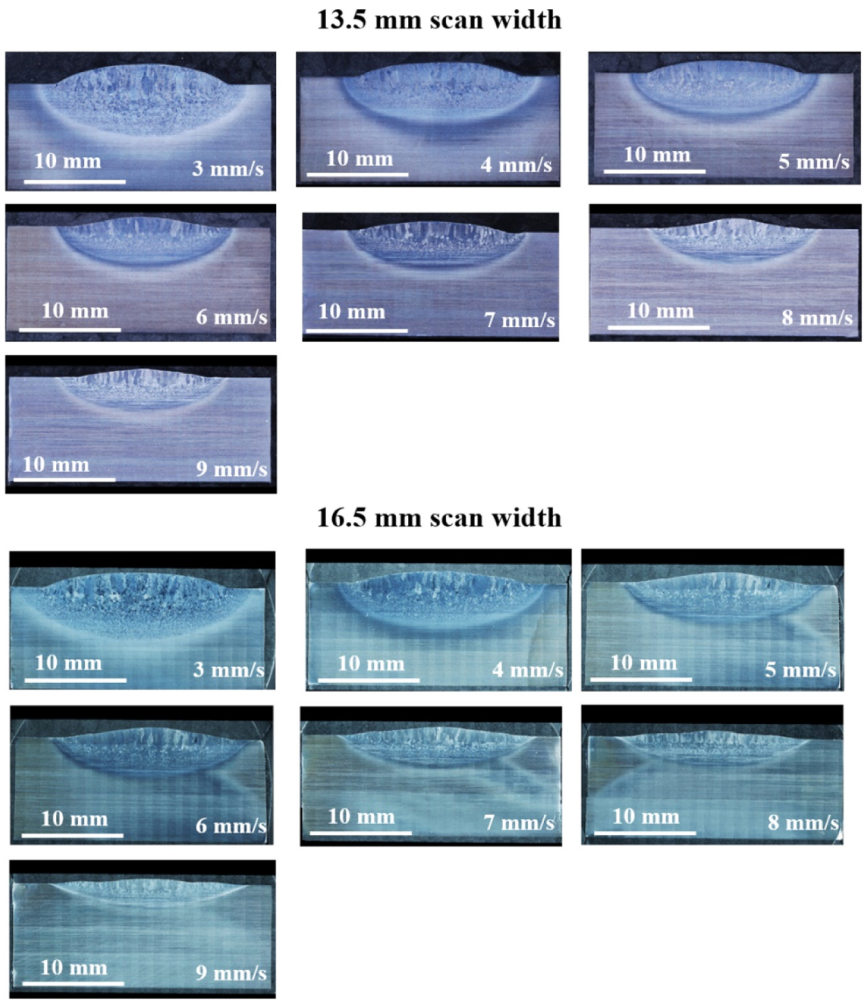


Fig. 14. Etched macrographs of deposited specimens with reduction energy per unit area (T) Scan width = 13.5 mm (B) Scan width = 16.5 mm.

Table 5
Bead geometry and energy per unit area of EPU 1 specimens.

Scan width (mm)	13.5	13.5	13.5	13.5	**13.5**	13.5	13.5
Travel speed (mm)	3.0	4.0	5.0	6.0	7.0	8.0	9.0
Width (mm)	16.84	16.16	15.43	14.02	**13.66**	12.60	12.32
Height (mm)	1.96	1.42	1.28	1.01	0.91	0.85	0.79
Penetration depth (mm)	1.39	0.73	0.66	0.57	0.54	0.52	0.59
Energy per unit area (J/cm^2)	6667	5000	4000	3333	**2857**	2500	2222

Table 6
Bead geometry and energy per unit area of EPU 2 specimens.

Scan width (mm)	16.5	16.5	16.5	**16.5**	16.5	16.5	16.5
Travel speed (mm)	3.0	4.0	5.0	6.0	7.0	8.0	9.0
Width (mm)	18.70	17.72	17.07	**16.78**	15.94	15.72	15.44
Height (mm)	1.55	1.18	1.15	0.85	0.81	0.73	0.52
Penetration depth (mm)	1.16	1.08	0.90	0.87	0.84	0.59	0.58
Energy per unit area (J/cm^2)	5454	4091	3273	**2727**	2338	2045	1818

improved process efficiency [6]. The slight reduction in penetration depth in the 16.5 mm specimens as compared to the 13.5 mm specimens may be a result of the larger melt pool surface area interaction with the substrate providing a larger area for conduction, more effectively drawing heat away from the melt pool. However, this phenomenon requires further investigation and more likely requires a larger separation between the arc and laser to be effective.

4. Conclusions

The outcome of these combined studies demonstrated that the laser-arc MES proposed by Chen et al. [13] to deposit mild steel, is applicable to the deposition of Ti-6Al-4V for the purpose of additive manufacturing. Additionally, this could be extended to welding applications. Fundamental process considerations have been made to enable successful deposition, however, additional studies to quantify the full effects of

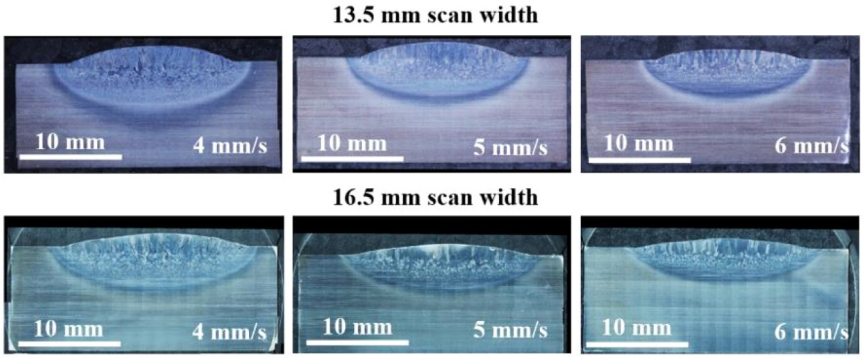


Fig. 15. Macrographs of central cross-sections of 3-line scan strategy Ti-6Al-4V deposits, utilising equivalent parameters to EPU 1 and EPU 2 for 13.5 mm and 16.5 mm scan width at 4 mm/s, 5 mm/s and 6 mm/s travel speed.

Table 7
Bead geometry of single line study EPU 1 compared with multi 3line strategy of equivalent process parameters at 13.5 mm scan width.

Scan strategy (SL – single line 3 L – 3 line strategy)	SL	3 L	SL	3 L	SL	3 L
Travel speed (mm/s)	4	4	5	5	6	6
Height (mm)	1.42	1.49	1.28	1.35	1.01	1.04
Width (mm)	16.16	16.05	15.43	15.09	14.02	14.15
Penetration depth (mm)	0.73	0.78	0.66	0.72	0.57	0.62
Primary HAZ depth (mm)	2.96	3.03	2.4	2.44	2.18	2.07

Table 8
Bead geometry of single line study EPU 2 compared with multi 3-line strategy of equivalent process parameters at 16.5 mm scan width.

Scan strategy (SL – single line 3 L – 3-line strategy)	SL	3 L	SL	3 L	SL	3 L
Travel speed (mm/s)	4	4	5	5	6	6
Height (mm)	1.18	1.28	1.15	1.10	0.85	0.98
Width (mm)	17.72	18.04	17.07	17.01	16.78	16.95
Penetration depth (mm)	1.08	0.91	0.90	0.74	0.87	0.64
Primary HAZ depth (mm)	2.58	2.52	1.93	1.99	1.99	1.69

varying process conditions need to be considered. The process demonstrated is a useful tool to enable the independent control of melt pool geometry from thermal input, a key limitation of any single energy source process. The process has many capabilities that should be investigated including dynamic width control, deposition of complex components and importantly multi-layer deposition for additive manufacturing. As well as enabling investigation into grain structure control of Ti-6Al-4V through manipulation of melt pool shape for a fixed thermal input as posited by Davis et al. [32].

In summary:

1) The MES process initially proposed [13] to deposit mild steel can be successfully applied to the deposition of Ti-6Al-4V. Utilizing a scanning laser and plasma arc to manipulate melt-pool shape, thus, bead geometry independently of thermal input.
2) Utilizing the geometric bead geometry prediction equation before deposition, the bead width and bead height can be independently controlled via simple processing parameters, allowing the user to deposit at the desired shape.
3) The penetration depth and primary HAZ at the center of the scanning path can be manipulated via a multi-speed scan strategy of the laser heat source, through removal of laser energy at the scan path center improving process efficiency.
4) The energy per unit area is a control factor to ensure that the desired scan width is achieved and devoid of defects. When the energy per unit area is too great the melt pool exceeds the desired scan width, too low, the melt pool generated is smaller than the scan width.

CRediT authorship contribution statement

Jialuo Ding: Writing – review & editing, Supervision, Resources, Project administration, Methodology, Funding acquisition, Conceptualization. **Wainwright James Christopher Julian:** Writing – original draft, Visualization, Validation, Software, Project administration, Methodology, Investigation, Formal analysis, Data curation, Conceptualization. **Alec Davis:** Writing – review & editing. **David Rico Sierra:** Writing – review & editing, Software, Investigation. **Stewart Williams:** Writing – review & editing, Supervision, Resources, Project administration, Methodology, Funding acquisition, Conceptualization.

Funding

The work was funded by the Engineering and Physical Science Research Council (EPSRC) [grant number: EP/R027218/1].

Declaration of Competing Interest

The authors declare that they have no known competing financial interests or personal relationships that could have appeared to influence the work reported in this paper.

Acknowledgements

The authors would like to express their gratitude to BAE Systems and the Engineering and Physical Science Research Council (EPSRC) for supporting this research via NEWAM [grant number: EP/R027218/1]. The technical teams at the Welding and Additive Manufacturing Centre at Cranfield University and the University of Manchester. The authors would like to express their gratitude to John Thrower and Mark Allen in assisting with experimental setup, Steve Pope and Tracey Roberts for support polishing and etching samples.

Data availability

Data is available through the Cranfield University Research Data Repository 'CORD' at https://doi.org/10.57996/cran.ceres-2737

References

[1] Williams SW, Martina F, Addison AC, Ding J, Pardal G, Colegrove P. Wire + arc additive manufacturing. Mater Sci Technol 2016;32(7):641–7. https://doi.org/10.1179/1743284715Y.0000000073.
[2] Frazier WE. Metal additive manufacturing: a review. J Mater Eng Perform 2014;23(6):1917–28. https://doi.org/10.1007/s11665-014-0958-z.

[3] Priarone PC, Pagone E, Martina F, Catalano AR, Settineri L. Multi-criteria environmental and economic impact assessment of wire arc additive manufacturing. CIRP Ann 2020;69(1):37–40. https://doi.org/10.1016/j.cirp.2020.04.010.
[4] Li JZ, Alkahari MR, Rosli NAB, Hasan R, Sudin MN, Ramli FR. Review of wire arc additive manufacturing for 3D metal printing. Int J Autom Technol 2019;13(3):346–53. https://doi.org/10.20965/ijat.2019.p0346.
[5] Jafari D, Vaneker THJ, Gibson I. Wire and arc additive manufacturing: opportunities and challenges to control the quality and accuracy of manufactured parts. Mater Des 2021;202. https://doi.org/10.1016/j.matdes.2021.109471.
[6] Wang C. High deposition rate wire based additive manufacture of Ti-6Al-4V. Cranfield University; 2020.
[7] Martina F, Mehnen J, Williams SW, Colegrove P, Wang F. Investigation of the benefits of plasma deposition for the additive layer manufacture of Ti–6Al–4V. J Mater Process Technol 2012;212(6):1377–86. https://doi.org/10.1016/j.jmatprotec.2012.02.002.
[8] Nilsiam Y, Sanders P, Pearce J. Applications of open source GMAW-based metal 3-D printing. J Manuf Mater Process 2018;2(1):18. https://doi.org/10.3390/jmmp2010018.
[9] Bai JY, Yang CL, Lin SB, Dong BL, Fan CL. Mechanical properties of 2219-Al components produced by additive manufacturing with TIG. Int J Adv Manuf Technol 2016;86(1–4):479–85. https://doi.org/10.1007/s00170-015-8168-x.
[10] Miguel, P., Almeida, S., Almeida, P.M.S., and Williams, S., 2010, "Innovative Process Model of Ti-6Al-4V Additive Layer Manufacturing Using Cold Metal Transfer (CMT)." [Online]. Available: ⟨https://www.researchgate.net/publication/51999200⟩.
[11] Wang F, Williams S, Rush M. Morphology investigation on direct current pulsed gas tungsten arc welded additive layer manufactured Ti6Al4V alloy. Int J Adv Manuf Technol 2011;57(5–8):597–603. https://doi.org/10.1007/s00170-011-3299-1.
[12] Lin JJ, Lv YH, Liu YX, Xu BS, Sun Z, Li ZG, et al. Microstructural evolution and mechanical properties of Ti-6Al-4V wall deposited by pulsed plasma arc additive manufacturing. Mater Des 2016;102:30–40. https://doi.org/10.1016/j.matdes.2016.04.018.
[13] Chen G, Williams S, Ding J, Wang C, Suder W. Multi-Energy Source (MES) configuration for bead shape control in wire-based directed energy deposition (w-DED). J Mater Process Technol 2022;304:117549. https://doi.org/10.1016/j.jmatprotec.2022.117549.
[14] Nayir S, Keist JS, Palmer TA. Role of changes in heat input on additively manufactured Ti–6Al–4V fabricated by directed energy deposition. Mater Sci Eng A 2021;822. https://doi.org/10.1016/j.msea.2021.141541.
[15] Xian G, Oh J mok, Lee J, Cho SM, Yeom JT, Choi Y, et al. Effect of heat input on microstructure and mechanical property of wire-arc additive manufactured Ti-6Al-4V alloy. Weld World 2022;66(5):847–61. https://doi.org/10.1007/s40194-021-01248-3.
[16] Feier A, Buta I, Florica C, Blaga L. Optimization of wire arc additive manufacturing (WAAM) process for the production of mechanical components using a CNC machine. Materials 2023;16(1). https://doi.org/10.3390/ma16010017.
[17] Khayoon MA, Hubeatir KA, Al-Khafaji MM. Laser transmission welding is a promising joining technology technique - A recent review. Journal of Physics: Conference Series. IOP Publishing Ltd; 2021. https://doi.org/10.1088/1742-6596/1973/1/012023.
[18] Mayi YA, Dal M, Peyre P, Bellet M, Fabbro R. Physical mechanisms of conduction-to-keyhole transition in laser welding and additive manufacturing processes. Opt Laser Technol 2023;158. https://doi.org/10.1016/j.optlastec.2022.108811.
[19] Ma S, Jiang M, Chen X, Li B, Jiang N, Chen Y, et al. Macro/micro-structure and mechanical properties of Al-6Mg-0.3Sc alloy fabricated by oscillating laser-arc hybrid additive manufacturing. J Alloy Compd 2022;929. https://doi.org/10.1016/j.jallcom.2022.167325.
[20] Mackenzie JK, Thomson MJ. Some statistics associated with the random disorientation of cubes. Biometrika 1957;44(1/2):205. https://doi.org/10.2307/2333253.
[21] Gong M, Meng Y, Zhang S, Zhang Y, Zeng X, Gao M. Laser-arc hybrid additive manufacturing of stainless steel with beam oscillation. Addit Manuf 2020;33. https://doi.org/10.1016/j.addma.2020.101180.
[22] Kapil A, Suga T, Tanaka M, Sharma A. Towards hybrid laser-arc based directed energy deposition: understanding bead formation through mathematical modeling for additive manufacturing. J Manuf Process 2022;76:457–74. https://doi.org/10.1016/j.jmapro.2022.02.027.
[23] Wang C, Suder W, Ding J, Williams S. Bead shape control in wire based plasma arc and laser hybrid additive manufacture of Ti-6Al-4V. J Manuf Process 2021;68:1849–59. https://doi.org/10.1016/j.jmapro.2021.07.009.
[24] Pardal G, Martina F, Williams S. Laser stabilization of GMAW additive manufacturing of Ti-6Al-4V components. J Mater Process Technol 2019;272:1–8. https://doi.org/10.1016/j.jmatprotec.2019.04.036.
[25] Wang C, Suder W, Ding J, Williams S. Wire based plasma arc and laser hybrid additive manufacture of Ti-6Al-4V. J Mater Process Technol 2021;293. https://doi.org/10.1016/j.jmatprotec.2021.117080.
[26] Hao K, Li G, Gao M, Zeng X. Weld formation mechanism of fiber laser oscillating welding of austenitic stainless steel. J Mater Process Technol 2015;225:77–83. https://doi.org/10.1016/j.jmatprotec.2015.05.021.
[27] Brooks RF, Dinsdale AT, Quested PN. The measurement of viscosity of alloys - a review of methods, data and models. Meas Sci Technol 2005;16(2):354–62. https://doi.org/10.1088/0957-0233/16/2/005.
[28] Mohr M, Wunderlich R, Novakovic R, Ricci E, Fecht H-J. Precise measurements of thermophysical properties of liquid Ti–6Al–4V (Ti64) alloy on board the international space station. Adv Eng Mater 2020;22(7). https://doi.org/10.1002/adem.202000169.
[29] Bellé MR, Neubert L, Sherstneva A, Yamamoto T, Nishi T, Yamano H, et al. Density, surface tension, and viscosity of liquid low-sulfur manganese–boron steel via maximum bubble pressure and oscillating crucible Methods. Steel Res Int 2025;96(5). https://doi.org/10.1002/srin.202400252.
[30] Biswas P, Mandal NR, Sha OP, Mahapatra MM. Thermo-mechanical and experimental analysis of double pass line heating. J Mar Sci Appl 2011;10(2):190–8. https://doi.org/10.1007/s11804-011-1059-0.
[31] Wunderlich R K. Surface tension and viscosity of industrial Ti-alloys measured by the oscillating drop method on board parabolic flights. High Temp Mater Process 2008;27(6). https://doi.org/10.1515/HTMP.2008.27.6.401.
[32] Davis AE, Wainwright J, Sahu VK, Dreelan D, Chen X, Ding J, et al. Achieving a columnar-to-equiaxed transition through dendrite twinning in high deposition rate additively manufactured titanium alloys. Metall Mater Trans A 2024;55(6):1765–87. https://doi.org/10.1007/s11661-024-07388-7.
[33] Chen G, Ding J, Sun Y, Chen X, Wang C, Pardal GR, et al. Efficient reduced-order thermal modelling of scanning laser melting for additive manufacturing. J Mater Process Technol 2023;321:118163. https://doi.org/10.1016/j.jmatprotec.2023.118163.
[34] Keller M, Chaudhary A, Kelly S, Medieros S. Absorption coefficient characterization in Ti-6Al-4V laser additive manufacturing. ICALEO 2006 - 25th International Congress on Applications of Laser and Electro-Optics, Congress Proceedings. Laser Institute of America; 2006. https://doi.org/10.2351/1.5060759.
[35] Kaplan AFH. Laser absorptivity on wavy molten metal surfaces: categorization of different metals and wavelengths. J Laser Appl 2014;26(1):012007. https://doi.org/10.2351/1.4833936.
[36] Wang C, Suder W, Ding J, Williams S. The effect of wire size on high deposition rate wire and plasma arc additive manufacture of Ti-6Al-4V. J Mater Process Technol 2021;288:116842. https://doi.org/10.1016/j.jmatprotec.2020.116842.
[37] Ríos S, Colegrove PA, Williams SW. Metal transfer modes in plasma wire + arc additive manufacture. J Mater Process Technol 2019;264(August 2018):45–54. https://doi.org/10.1016/j.jmatprotec.2018.08.043.
[38] Brandl E, Michailov V, Viehweger B, Leyens C. Deposition of Ti-6Al-4V using laser and wire, part I: microstructural properties of single beads. Surf Coat Technol 2011;206(6):1120–9. https://doi.org/10.1016/j.surfcoat.2011.07.095.
[39] Wang F, Williams S, Colegrove P, Antonysamy AA. Microstructure and mechanical properties of wire and arc additive manufactured Ti-6Al-4V. Metall Mater Trans A 2013;44(2):968–77. https://doi.org/10.1007/s11661-012-1444-6.
[40] Gisario A, Kazarian M, Martina F, Mehrpouya M. Metal additive manufacturing in the commercial aviation industry: a review. J Manuf Syst 2019;53(August):124–49. https://doi.org/10.1016/j.jmsy.2019.08.005.
[41] Zheng B, Jiang G, Wang W, Wang K, Mei X. Ablation experiment and threshold calculation of titanium alloy irradiated by ultra-fast pulse laser. AIP Adv 2014;4(3). https://doi.org/10.1063/1.4867088.
[42] Dinovitzer M, Chen X, Laliberte J, Huang X, Frei H. Effect of wire and arc additive manufacturing (WAAM) process parameters on bead geometry and microstructure. Addit Manuf 2019;26:138–46. https://doi.org/10.1016/j.addma.2018.12.013.
[43] Addison, A., Ding, J., Martina, F., Lockett, H., and Williams, S., 2015, "Manufacture of Complex Titanium Parts Using Wire + Arc Additive Manufacture," Titanium Europe 2015, Brimingham.
[44] Lin Z, Song K, Yu X. A review on wire and arc additive manufacturing of titanium alloy. J Manuf Process 2021;70:24–45. https://doi.org/10.1016/j.jmapro.2021.08.018.
[45] Neto L, Williams S, Ding J, Hönnige J, Martina F. Mechanical properties enhancement of additive manufactured Ti-6Al-4V by machine hammer peening. Lect Notes Mech Eng 2020:121–32. https://doi.org/10.1007/978-981-15-0054-1_13.



https://dspace.org/

Melt pool geometry control of Ti-6Al-4V utilizing multi-energy source laser-arc + wire directed energy deposition

Wainwright, James; Sierra, David Rico; Davis, Alec E.; Williams, Stewart; Ding, Jialuo

2026-02
Elsevier
https://doi.org/10.1016/j.cirpj.2025.11.008
Wainwright J, Sierra DR, Davis A, et al., (2026) Melt pool geometry control of Ti-6Al-4V utilizing multi-energy source laser-arc + wire directed energy deposition. CIRP Journal of Manufacturing Science and Technology, Volume 64, February 2026, pp. 79-91

Downloaded from a DSpace repository. https://dspace.org/